

Seeded Topology Optimization for Commercial Foundry Integrated Photonics

JACOB M. HIESENER¹, C. ALEX KAYLOR¹, JOSHUA J. WONG¹,
PRANKUSH AGARWAL¹, STEPHEN E. RALPH^{1,*}

¹*School of Electrical and Computer Engineering, Georgia Institute of Technology, Atlanta, GA 30308, USA*
^{*}*stephen.ralph@ece.gatech.edu*

Abstract:

We present a seeded topology optimization methodology for integrated photonic devices fabricated on foundry platforms that yields improved performance compared to traditional topology optimization. We employ blurring filters and a DRC correction algorithm to more readily meet design rule checks yielding devices with fewer artifacts and improved correlation between simulation and measurements. We apply this process to an ultra-compact TE modal multiplexer, a TE mode converter, a polarization rotator, and a high-contrast grating reflector. The measured insertion loss of the TE mode converter was reduced from 1.37 dB to 0.64 dB through this optimization strategy. This approach enables the use of physics-informed device topologies in inverse design and maintains compliance to foundry constraints throughout optimization.

1. Introduction

Inverse design is a rapidly evolving method that is used in the design and optimization of integrated photonic devices to create compact structures with record performance that exploit non-intuitive geometries. Density-based topology optimization (TO) is a flexible form of inverse design that allows each voxel of a design (design parameters) to continuously evolve between two or more materials towards an optimal device topology [1–4]. In density-based TO, two or more Maxwell simulations are performed each iteration to determine gradients of the design parameters with respect to one or more user-specified figures of merit (FOM) using the adjoint variable method [1, 5]. The gradients are linearly combined to update the design region toward a locally optimum topology.

Devices designed for fabrication at a commercial foundry can be manufactured at high volumes after a successful validation process. This ability to scale is achieved by the requirement that devices conform to stringent design rules checks (DRC) to ensure accurate fabrication with high yield [6]. We can exploit the gradient descent method used in TO by generating gradients that iterate the design to a condition where design rules are met. In our TO pipeline, we have previously implemented algorithms that calculate gradients to meet geometric linewidth constraints (GLC) and area constraints (AC) which are then linearly combined with the FOM gradient each iteration [7].

In traditional TO methodologies, the design parameters are gray-scale i.e., allowed to take on any material value between the two or more materials available on that layer in the material stack. However, to accurately detect DRC violations in a device topology, the device must be sufficiently binary (i.e. every voxel is close to 0 (void) or 1 (solid)) making it challenging to effectively apply DRC constraints. When binarizing the design parameters, a locally optimum topology in the gray-scale phase of the optimization may not translate to a locally optimum binary topology, resulting in a reduction in performance in late stages of TO. This effect is amplified when fabrication-based constraints are included in the optimization, as conflicting gradients (FOM vs. AC/GLC) may cause the optimizer to stall when evolving the geometry to satisfy DRC results in a drop in performance [8, 9]. Hence, there is a need for a modified topology optimization algorithm that maintains device fabricability while exploring the local design space around a functional seed geometry.

In this work we present a seeded TO methodology in which a known functional device geometry, the seed, is iteratively processed and optimized using density-based TO achieving performance beyond the capabilities of traditional TO. A limited blurring filter is applied to enable perturbation of the topology such that the design space around the seed can be explored. We develop a DRC correction algorithm that is catered to the seeded TO process which efficiently resolves foundry constraints while allowing TO to improve device performance. While TO has the potential to discover completely novel geometries, seeded TO focuses efforts to create strictly fabricable devices. We note that the seed can originate from physics-based conventional design strategies. An example is the seeded optimization of high-contrast gratings (HCGs) originally designed using parameter optimization [10, 11]. Shape optimization is a similar inverse design methodology in which a user defines a boundary that is adjusted throughout optimization to maximize performance [12, 13]; however our design methodology allows for changes in the device topology (i.e., elimination and creation of holes/islands) and includes our highly effective DRC correction algorithm. We apply seeded TO to foundry-fabricated inverse designed devices and present an improved design pipeline that utilizes the global optimization features of density-based TO along with the refined, local optimization capability of seeded TO.

2. Topology Optimization Overview

Density-based TO parameterizes the design region such that each voxel can vary between "solid" (high index material) and "void" (low index material) between the two or more materials available on that layer. Typically, every voxel in the design region is initialized to 0.5, meaning the permittivity is halfway between the solid (1) and the void (0) so each voxel can evolve to either. The user specifies the design region lateral dimensions, the location and size of all optical input and output ports (typically waveguides but coupling to a fiber is another example), sources and monitors, and formulates one or more FOMs to minimize. Our unique solver is a hybrid time/frequency-domain adjoint-variable method that readily enables solutions across a wide spectrum via the open-source finite-difference time-domain (FDTD) maxwell solver MEEP [14]. This method allows for the inclusion of multiple FOMs for a single device and enables constraint-based TO [7].

In addition to the FOM-based gradients, multiple DRC-based gradients are used to optimize for GLC (minimum linewidth and linespacing) and AC (minimum area and enclosed area) in our TO pipeline. The gradient for GLC is generated using a chosen set of erosions and dilations that identify inflection regions which violate DRC, but can also be generated using morphological transforms [7, 15–18]. AC includes the minimum area and enclosed area which are implemented using an indicator function that identifies the problematic areas to generate a gradient that encourages the holes/islands to dilate or erode. The minimum curvature radius is another DRC constraint, however the curvature is implicitly enforced by the GLC implementation and the conic filter (w) used to map the design parameters [7].

To manage the trade-off between performance and foundry constraints we utilize user-set physical programming bounds that weight the effect of the performance-based FOM and foundry constraints (GLC, and AC) to create the final gradient used in each stage of the optimization [19, 20]. This allows the designer to increase the effect of constraints on the gradient which helps to prevent the optimization from stalling by favoring DRC compliance. These bounds are critical to ensuring the final device is DRC clean but often require hyperparameter tuning through heuristic approaches to mitigate performance loss when AC and GLC physical programming bounds are reduced. Our seeded TO methodology relies less on these bounds, allowing streamlined, efficient optimization that maintains performance with foundry constraints applied.

2.1. Design Parameter Mapping

In order to map the latent design parameters (ρ) to permittivity values for simulation we use a density-based interpolation scheme. We first filter the design parameters:

$$\tilde{\rho} = w * \rho \quad (1)$$

where w is a conic filter and $\tilde{\rho}$ are the filtered design parameters [21]. The filtered design parameters are then projected using a differentiable, nonlinear function:

$$\bar{\rho} = \frac{\tanh(\beta\eta) + \tanh(\beta(\tilde{\rho} - \eta))}{\tanh(\beta\eta) + \tanh(\beta(1 - \eta))} \quad (2)$$

where β is a threshold parameter gradually increased throughout the optimization process to binarize the device, η is a threshold parameter set to 0.5, and $\bar{\rho}$ are the mapped design parameters [22]. The permittivity is interpolated from the mapped design parameters:

$$\epsilon_r(\bar{\rho}) = \epsilon_{min} + \bar{\rho}(\epsilon_{max} - \epsilon_{min}) \quad (3)$$

where the relative permittivity of each voxel ϵ_r varies between the void (ϵ_{min}) and solid permittivity (ϵ_{max}). This linear interpolation scheme works well for silicon photonic devices; however, nonlinear interpolation schemes may be more suitable for other design problems [23].

3. Seeded Topology Optimization

The goal of seeded TO is to take a known functional device geometry and improve performance based on a user-specified FOM while maintaining device fabricability. This requires careful processing of the seeded design parameters so the topology can be effectively enhanced using density-based TO. As an extreme example we use seeded TO to optimize a flawed seed with many DRC violations, achieving a fabricable, semi-functional device (Fig. 1a). The DRC violations make this seed ideal for demonstrating how seeded TO can improve device performance while achieving and maintaining DRC clean status. The test cases in this work use functional seeds that comply with DRC and have good initial performance to demonstrate the ability of seeded TO in finding superior local optima.

At the start of each iteration of seeded TO, the mapped design parameters ($\bar{\rho}$) are first fully binarized:

$$\sigma(\mathbf{r}) = \begin{cases} 0, & \bar{\rho}(\mathbf{r}) \leq 0.5 \\ 1, & \bar{\rho}(\mathbf{r}) > 0.5 \end{cases} \quad (4)$$

where σ is the binarized design parameters and \mathbf{r} is the position vector of a voxel (Fig. 1b). The blurred design parameters ($\tilde{\sigma}$) are then computed:

$$\tilde{\sigma} = w_b * \sigma \quad (5)$$

where w_b is a blurring filter that enables perturbation of the topology during TO. The filter is typically set to a box averaging filter of a user-specified size, however Gaussian filters have also been tested and shown to be effective. The DRC correction algorithm is then applied based on indicator functions used to identify locations in the device topology with DRC violations. The GLC violation indicators (minimum linewidth: I_{lw} , minimum linespacing: I_{ls}) are found using the open-source software imageruler [24, 25], while the AC indicators (minimum area: I_a , minimum enclosed area: I_{ea}) are determined using a contour detection algorithm [7]. The DRC corrected design parameters ($\tilde{\sigma}$) are:

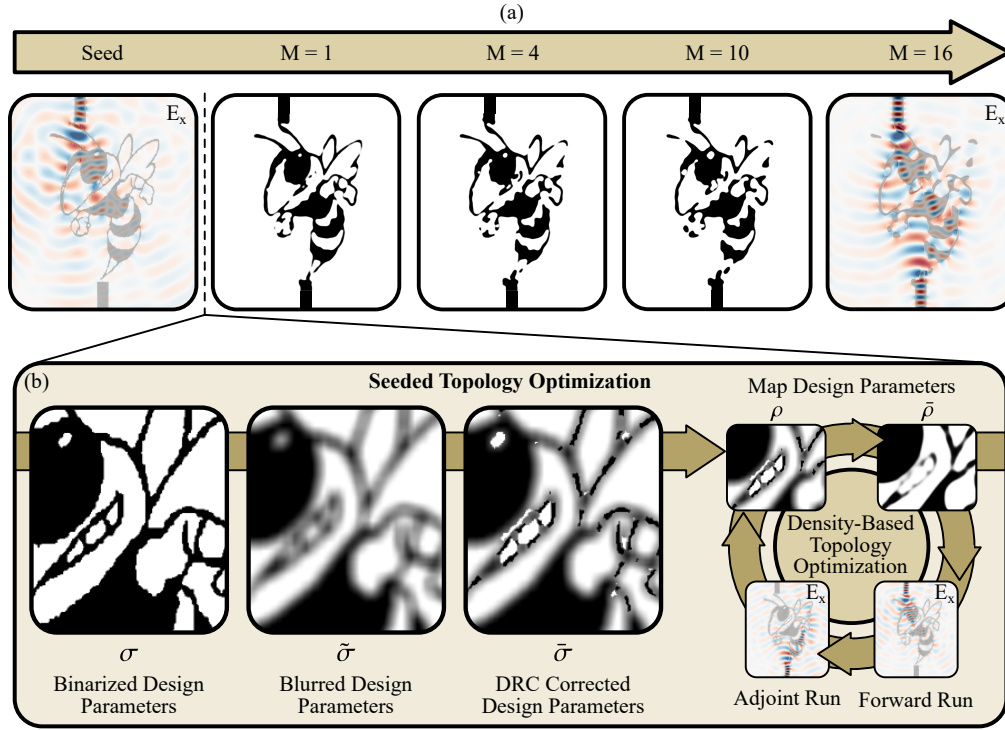


Fig. 1. Overview of the seeded TO process applied to a seed with poor initial performance and significant DRC violations. (a) 16 iterations (M) of seeded TO are applied to optimize transmission to an output waveguide. (b) Overview of one iteration of seeded TO. First, a blurring filter is applied to the binarized design parameters (σ) to allow the edges of the device to be perturbed during topology optimization. Second, a DRC correction algorithm is applied to the blurred design parameters ($\tilde{\sigma}$), adding material in areas violating minimum linewidth/area and removing material in areas violating minimum line-spacing/enclosed area. Finally, design parameters of TO (ρ) are set to the DRC corrected design parameters ($\bar{\sigma}$) and multiple iterations of density-based TO are applied to the device.

$$\bar{\sigma}(\mathbf{r}) = \begin{cases} 0, & \mathbf{r} \in I_{ls}, I_{ea} \\ 1, & \mathbf{r} \in I_{lw}, I_a \\ \tilde{\sigma}, & \text{otherwise} \end{cases} \quad (6)$$

This expands or dilates regions in the mapped topology to algorithmically force DRC compliance beyond inclusion of the constraints in TO. The latent design parameters (ρ) of TO are set to the filtered and processed design parameters and 10-20 iterations of TO are performed, allowing the topology to reach a new local minimum. AC and GLC optimization is included in the TO stage, ensuring the final device satisfies DRC. This cycle is repeated until a high-performing, DRC clean device is achieved (Fig. 1a).

3.1. Improved Inverse Design Pipeline

Our new design pipeline begins first with seed generation, this can be accomplished with a variety of tools including traditional TO wherein a device is first optimized with respect to the FOM in traditional TO, followed by optimization with foundry constraints, and completed with

seeded TO. This design evolution for a TE modal multiplexer (MMUX) is depicted in Fig. 2. A TE MMUX converts the fundamental mode of 2 single mode waveguides to the TE₀ and TE₁ modes in a multimode waveguide. In our traditional TO implementation the threshold parameter β is typically increased every 20 iterations to slowly binarize the design parameters while the optimizer minimizes the objective function (Fig. 2a) [1]. Before foundry constraints are applied, the FOM often achieves a minimum as the design region is not fully binary (Fig. 2c). AC and GLC optimization is included in the later stages of TO, resulting in reduced performance as the device binarizes and adjusts to satisfy DRC. When constraints are added to TO, the GLC implementation causes the device to binarize but may leave some AC violations (Fig. 2d). To resolve the AC violations, the user set physical programming constraint bounds are further restricted, causing the optimizer to focus on AC over the FOM (Fig. 2e).

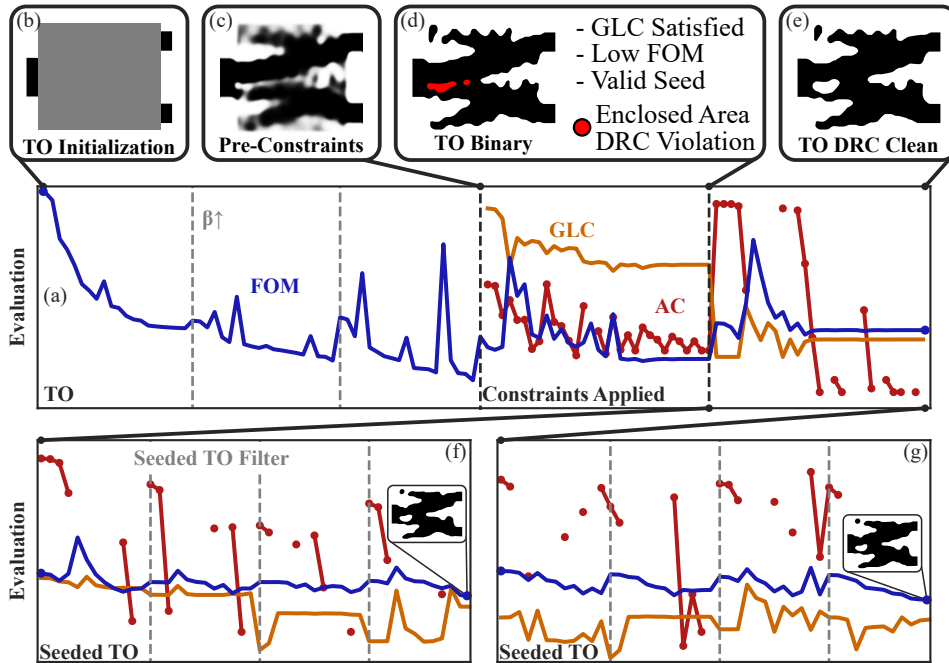


Fig. 2. (a) TO evolution of a TE modal multiplexer. Initially the design region is set to uniform gray area (b) and optimized solely for the FOM(s) with β increasing every 20 iterations to slowly binarize the device. Before the design is fully binarized, constraints are added to the optimization (AC: area constraint, GLC: geometric linewidth constraint) (c). This binarizes the device (d) and the hyperparameters are then tuned to force the device to satisfy DRC (e). Both binary devices ((f) TO binary and (g) TO DRC clean) are used as seeds for seeded TO where the design region is filtered every 12 TO iterations. If no contour detected by the AC algorithm violates DRC, AC is not applied; therefore the AC evaluation does not exist for some iterations.

The seed topology is not required to be DRC clean, but it must be binary. Seeded TO was performed on the MMUX 30 iterations after constraints are applied (Fig. 2f) and after TO achieves a DRC clean device (Fig. 2g) [9]. The FOM for both cases reduces throughout the optimization, however the AC and GLC evaluation was much lower for the MMUX seed that was DRC clean. The resulting MMUXs are almost identical, both satisfying DRC with similar performance. This allows the user to end TO early and achieve an optimal device topology, reducing the computational cost of an optimization.

3.2. Blurring Filter Study

The blurring filter used in seeded TO directly enables perturbation of the design parameters, making the size and shape of the filter critical in altering the overall device performance. Other filter shapes that convert a binary geometry to gray-scale are compatible with seeded TO, here we demonstrate the performance of the box filter with a user set X and Y size.

The size of the blurring filter significantly impacts the effectiveness of the seeded TO optimization. A small filter has limited ability to perturb the design parameters and therefore limits the design search space to near the seed device. If the filter is too large, small but critical features of the device are obscured and not necessarily recovered in subsequent optimization. An ideal filter size allows for the maximum design region perturbation without eliminating functional features. The size and shape of the optimal filter may vary depending on device and material platform and will require tuning, however a practical starting size is one quarter of the single-mode waveguide width for the material platform being used. Naively, it may appear that the filter size should be on the order of the minimum feature size from the foundry, but in reality, the dimensions are significantly more dependent on the material platform being optimized. For example, silicon nitride designs would require a larger filter size than the devices in this work, but silicon devices from two foundries with different DRC constraints would have similar optimal filter dimensions.

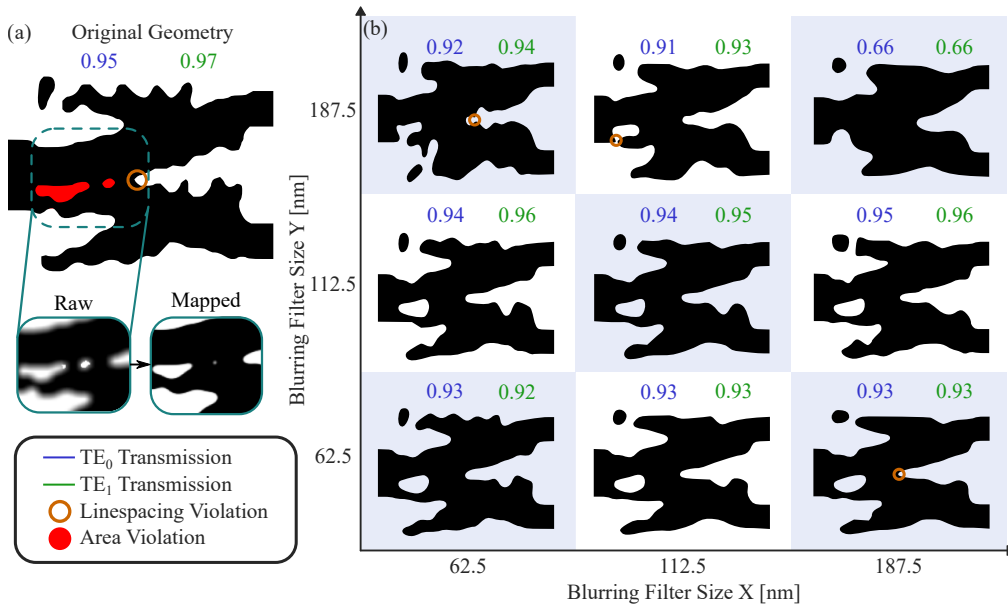


Fig. 3. (a) Traditional TO was used to design a $2.4 \times 2.4 \mu\text{m}$ modal multiplexer in a 2D simulation environment which contains DRC violations. In seeded TO the design parameters are blurred with a DRC correction algorithm applied. Identical to pure TO, the parameters are passed through a mapping function to return the permittivity values to be used in the Maxwell simulation. (b) Comparison of varying box filter dimensions used for the seeded TO blurring filter with DRC violations highlighted.

To investigate the effect of filter size on device performance, a blurring filter study was performed on a 2D ultra-compact MMUX designed using traditional TO to create the seed (Fig. 3a). X and Y filter sizes of 62.5, 112.5, and 187.5 nm were selected for the filter study. The MMUX optimized with the 112.5×112.5 nm blurring filter has excellent performance, however the asymmetric 187.5×112.5 nm filter exhibited slightly better performance. This

asymmetric filter has increased blur along the X-axis, which likely elongates the hole at the multimode-waveguide interface without eliminating it, enhancing the TE_1 conversion efficiency. Other size filters had either reduced performance or DRC errors due to elimination of critical features or minimal design parameter perturbation respectively. Though the choice of filter size is critical to seeded TO performance, there are no other additional hyperparameters introduced to the optimization enabling seamless transition between traditional TO and seeded TO. The original hyperparameters, such as the physical programming bounds and thresholding parameters, have less effect on a seeded TO optimization due to the device topology being binary and require less tuning for an effective optimization.

4. Test Cases

To demonstrate seeded TO we optimize an ultra-compact MMUX [9], a mode converter [26], and a polarization rotator [27], each initially optimized using traditional TO. We also demonstrate the design of a high contrast grating (HCG) reflector initially optimized using a parameter optimization (PO) method [10]. All of these devices are designed for the GlobalFoundries silicon photonics process (GF45CLO).

4.1. Modal Multiplexer

The use of higher order optical modes in integrated photonics has many applications including photonic computation, high extinction/low loss switching systems, and high data-rate communications using mode-division multiplexing [28–30]. In these systems, a MMUX or mode converter is required to couple between modes. We use seeded TO to improve an ultra-compact ($3 \times 3 \mu\text{m}$) MMUX designed with traditional TO (Fig. 4a) [9]. This device converts the fundamental mode of two separate waveguides to the TE_0 and TE_1 modes in a multimode waveguide (Fig. 4b,c) [17].

The original design uses both the silicon and polysilicon layers offered by the GF45CLO process to maximize the number of design parameters available in a compact design region. However, after analysis of experimental results, simulations propounded that the polysilicon layer was not required for an optimal MMUX design [8]. Omitting the polysilicon layer from the original MMUX had negligible effect on simulated device performance, therefore that layer was removed before performing seeded TO.

This device requires parallel optimization of both the TE_0 and TE_1 performance which are defined by the following FOMs:

$$FOM_{TE_0} = \left(1 - \frac{P_A}{P_0}\right) + \alpha \frac{P_B}{P_0}, \quad FOM_{TE_1} = \left(1 - \frac{P_B}{P_1}\right) + \alpha \frac{P_A}{P_1} \quad (7)$$

α is the extinction coefficient, P_k is the input power of the TE_k mode, P_A is the optical power in the single-mode waveguide A (port 1/4), and P_B is the optical power in the single-mode waveguide B (port 2/3) [9] (Fig. 4a). This is designed to both maximize transmission and minimize the extinction ration (ER).

Both devices were fabricated and measured using the back-to-back test structure shown in Fig. 4a. A standard fiber-array setup was used to perform wavelength scans with a tunable laser on each device using GF45CLO PDK grating couplers for optical input and output. The open-source photonic integrated circuit testing software LabExT was used to automate measurements [31]. Test structures for both MMUX designs are measured across six separate chips from two wafers and the S-parameters are compared to simulation (Fig. 4).

The S_{41} transmission encapsulates two passes through the MMUX for the TE_0 channel while the S_{32} transmission encapsulates two passes for the TE_1 channel. The S_{42} and S_{31} are the same due to reciprocity and capture the crosstalk between the TE_0 and TE_1 channels.

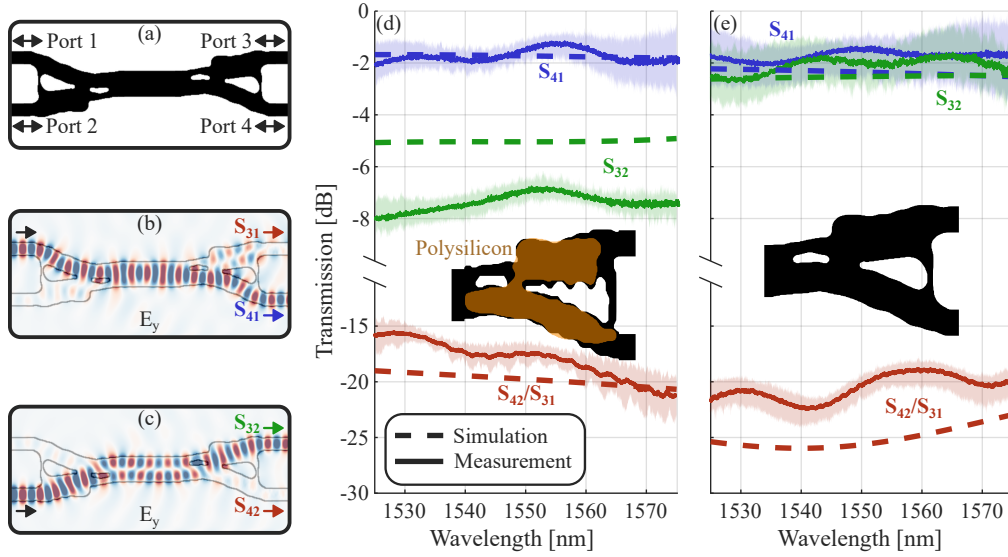


Fig. 4. (a) Measurement test structure for the modal multiplexer with labeled ports. (b) Field plot of the first measurement condition with light input through port 1, transmission measured through port 4, and crosstalk measured through port 3. (c) Field plot of the second measurement condition with light input through port 2, transmission measured through port 3, and crosstalk measured through port 4. The simulated and measured S-parameter spectra are plotted for the TO (d) and seeded TO (e) variants.

The traditional TO MMUX required post-TO manual modification to satisfy DRC, which involved expanding the hole near the multimode waveguide to satisfy the minimum area constraint [9]. These manual modifications move the device topology outside of a local optimum, causing a reduction in the TE_1 transmission in both simulation and measurement (Fig. 4d). By strict enforcement of DRC constraints through our DRC correction algorithm, seeded TO produces a topology that satisfies DRC with improved performance for both modes compared the the traditional TO design (Fig. 4e).

An asymmetric blurring filter is used in seeded TO for this device with a larger blur along the x-axis. This allows the DRC limited hole to stretch in x while preventing annihilation of the hole via a large y-axis blur, augmenting the mode conversion efficiency for the TE_1 case while maintaining DRC compliance. The final seeded TO topology is smoother than the traditional TO device without the periodic ripples that appear throughout the structure. The disparity in TE_1 simulated and measured transmission for the TO MMUX may be caused by the lithography process used to fabricate these devices which often smooths structures with sharp curvature and small features resulting in variation of device performance compared to simulation [32–34]. The seeded TO MMUX has fewer small, jagged features making it more suitable for the lithography process.

4.2. Mode Converter

The mode converter designed in this work converts the fundamental TE_0 mode in a single-mode waveguide to the TE_1 mode of a multimode waveguide in a compact ($6 \times 3 \mu\text{m}$) footprint. The traditional TO version of this device was designed to demonstrate compact, multimode structures for high power signal routing [26]. We apply seeded TO to this device to improve the mode conversion efficiency and reduce the modal crosstalk.

Like the MMUX, a TE mode converter is critical for any multimode system. The original

device was optimized with a TE_0 source in the single-mode waveguide and a TE_1 monitor in the output waveguide. The objective function was designed to only maximize TE_1 transmission. For the seeded TO device, a crosstalk term was added to the objective function to maximize extinction:

$$FOM = \left(1 - \frac{P_1}{P_{in}}\right) + \alpha \frac{P_0}{P_{in}} \quad (8)$$

α is the extinction coefficient (set to 10 for this optimization), P_m is the power of the m^{th} TE mode in the multimode waveguide, and P_{in} is the input power. This ensures the crosstalk of the final device is low while maximizing mode conversion efficiency. Seeded TO was performed using a square averaging filter instead of the asymmetric filter used for the MMUX.

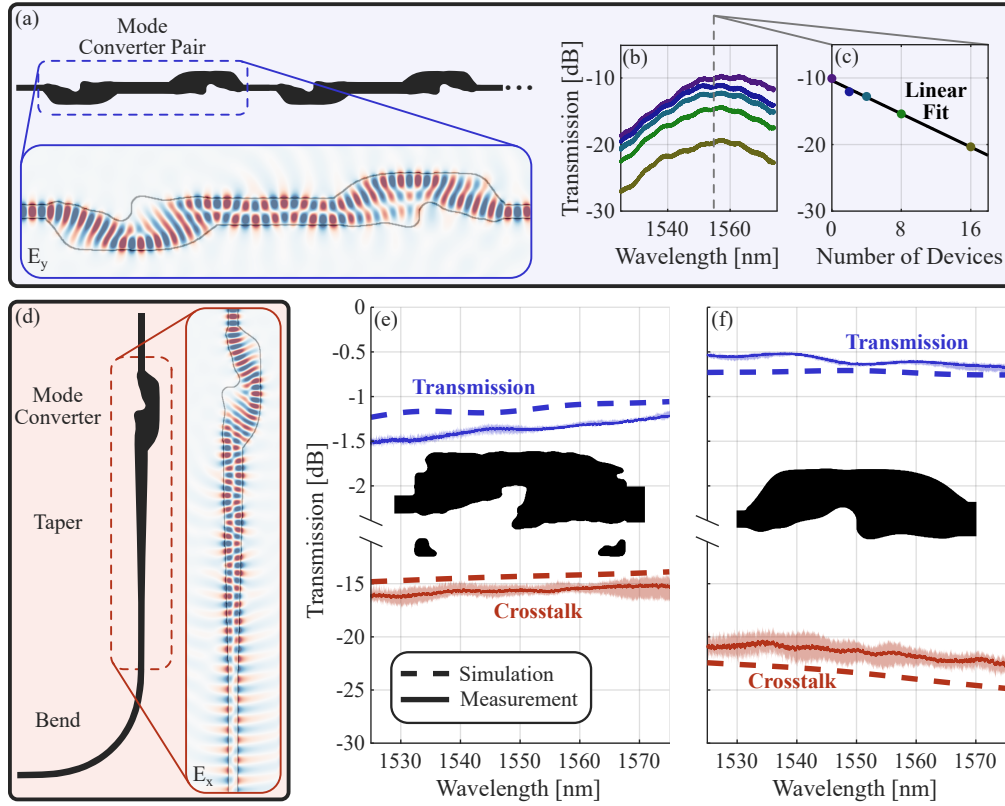


Fig. 5. (a) The transmission of the TE_0 to TE_1 mode converter is measured using test structures with a varying number of cascaded mode converter pairs. The transmission spectrum is measured for each test structure (b) and a linear fit is applied at each wavelength point (c) to find the loss per device (slope). (d) The crosstalk of the mode converter is measured by using a taper and bend to remove any power in higher order modes after the mode converter. The simulated and measured transmission and crosstalk spectra are plotted for the TO (e) and seeded TO (f) variants.

Test structures were designed to measure both the transmission and crosstalk of each mode converter. A standard fiber-array setup was used to perform wavelength scans on each test structure over the same wavelength span as the MMUX. The transmission measurement uses test structures with 0, 1, 2, 4, and 8 mode converter pairs (Fig. 5a). This allows us to apply a linear fit to the transmission vs. number of devices curve at each wavelength point, the slope of the

linear fit is the transmission through one device (Fig. 5b,c). For the crosstalk measurement, we measure a mode converter followed by a taper and a bend (Fig. 5d). The taper converts the TE_1 mode to a substrate mode that is lost through the bend. Any power in the fundamental mode after the mode converter is sustained through the taper and bend and measured to determine the crosstalk of the mode converter.

Similar to the Modal Multiplexer, the seeded TO mode converter developed much smoother edges than its traditional TO counterpart. The performance of the seeded TO design is also improved due to lower crosstalk and increased transmission in both simulated and measured data (Fig. 5e,f). The measured transmission of the TO device is roughly 0.4 dB lower than simulation. Like the MMUX, the traditional TO mode converter may also have a mismatch in performance due to lithographic smoothing. However, the seeded TO mode converter has slightly higher measured transmission compared to simulated. This indicates that features developed through seeded TO are more suitable to the fabrication process.

4.3. Polarization Rotator

A polarization rotator converts the fundamental TE mode to the fundamental TM mode in a single-mode waveguide. The original polarization rotator was designed using TO with a size of $8 \times 2 \mu\text{m}$ [27]. Polarization control in integrated photonics enables a variety of applications including polarization division multiplexing, medical sensing, and dispersion engineering [35–38]. To convert from TE to TM the direction of the \vec{E} and \vec{H} fields needs to rotate by 90° ; this can only be achieved using a structure that breaks z-symmetry, which the polysilicon layer on the GF45CLO process can be used for, making it crucial for an effective polarization rotator [27]. Both the silicon and polysilicon layers are optimized simultaneously throughout the TO process.

The objective function used to design the polarization rotator was designed solely to maximize the TE to TM conversion efficiency:

$$FOM = 1 - \frac{P_{TM}}{P_{in}} \quad (9)$$

Where P_{TM} is the power in the TM mode at the output and P_{in} is the input power. Simulation results reveal the seeded TO polarization rotator outperforms the TO polarization rotator in both crosstalk and transmission over C-band (Fig. 6a,b). Test structures for this device have been included in a future multi-process wafer tapeout.

Like the previous devices, seeded TO smoothed many of the ripples present in the traditional TO polarization rotator. The output waveguide is disconnected from the bulk of the TO device whereas the output waveguide is connected in the seeded TO variant. A shape optimization design methodology would not allow for disconnected features to merge, changing the device topology [12, 13]. The improvement made by seeded TO can be seen in the field plots where the magnitude of the E_y field is significantly reduced in the output waveguide of the seeded TO variant compared to the original TO device (Fig. 6c,d).

To investigate the robustness of seeded TO, we performed a layer misalignment study on the polarization rotator. The polysilicon layer was shifted in both X and Y with respect to the nominal position. Both devices are far more sensitive to layer misalignment in the Y-direction due to the small device width. The peak transmission for the TO polarization rotator is shifted 20 nm in X and 20 nm in Y from the nominal position whereas the peak transmission for the seeded TO device is shifted -10 nm in X and 10 nm in Y. This indicates that the seeded TO design is more robust to layer misalignment and a stronger local optimum. The smoothing feature of seeded TO appears to increase the robustness of resulting devices without including any robust-based design scheme in the optimization.

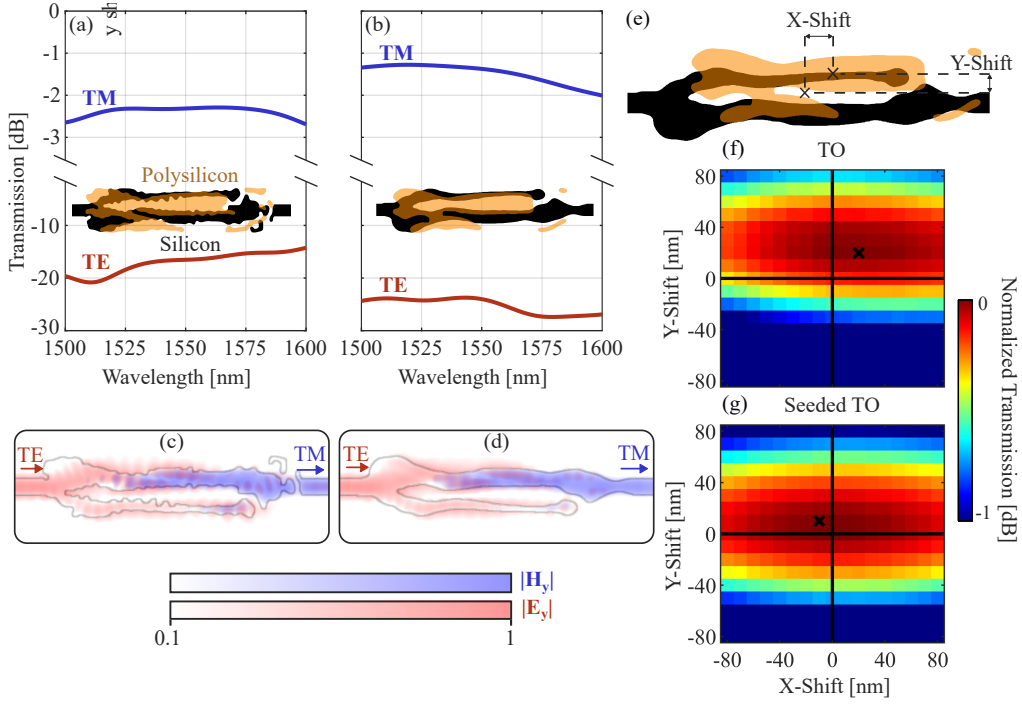


Fig. 6. Simulations reveal that TM transmission and TE extinction spectra are uniformly improved for the seeded TO (b) compared to the traditional TO design (a) of a polarization rotator. (c,d) Normalized log-scale field magnitudes show the rotation of the TE mode via the $|E_y|$ field (red) to the TM mode via the $|H_y|$ field (blue) for both devices. (e) A layer misalignment study was performed by shifting the polysilicon layer from the nominal position in both X and Y. Heat maps are generated for the polarization rotator transmission at 1550 nm normalized to the maximum transmission (marked with an "x") for the TO (f) and the STO (g) polarization rotator.

4.4. High Contrast Grating Reflector

Parameter optimization (PO) was used to generate a $4.5 \times 6 \mu\text{m}$ HCG to investigate the performance of seeded TO with a seed designed using alternative methods to TO. This HCG reflector is designed to reflect the fundamental mode of a single-mode waveguide with an ultra-compact footprint. These reflectors are fundamental in the design of many integrated photonic systems such as compact filters and integrated lasers [39]. The PO HCG consists of apodized concave gratings with a taper to shape the waveguide mode entering the grating region (Fig. 7f) [10]. The design of the PO HCG was based on other high contrast gratings such as grating couplers and circular grating reflectors [40]. Seeded TO was then applied to the PO structure to further improve the reflectance of the grating.

Mirror symmetry can be applied to this device about the $y = 0$ axis. The FOM used for the optimization of this device is to maximize transmission into the reflected mode:

$$FOM = 1 - \frac{P_r}{P_{in}} \quad (10)$$

P_r is the reflected power and P_{in} is the input power. To measure this device, a resonator was created using a directional coupler and two HCGs as mirrors (Fig. 7a). This device acts as an add/drop ring resonator due to the counter-propagating light in the resonator. The HCG

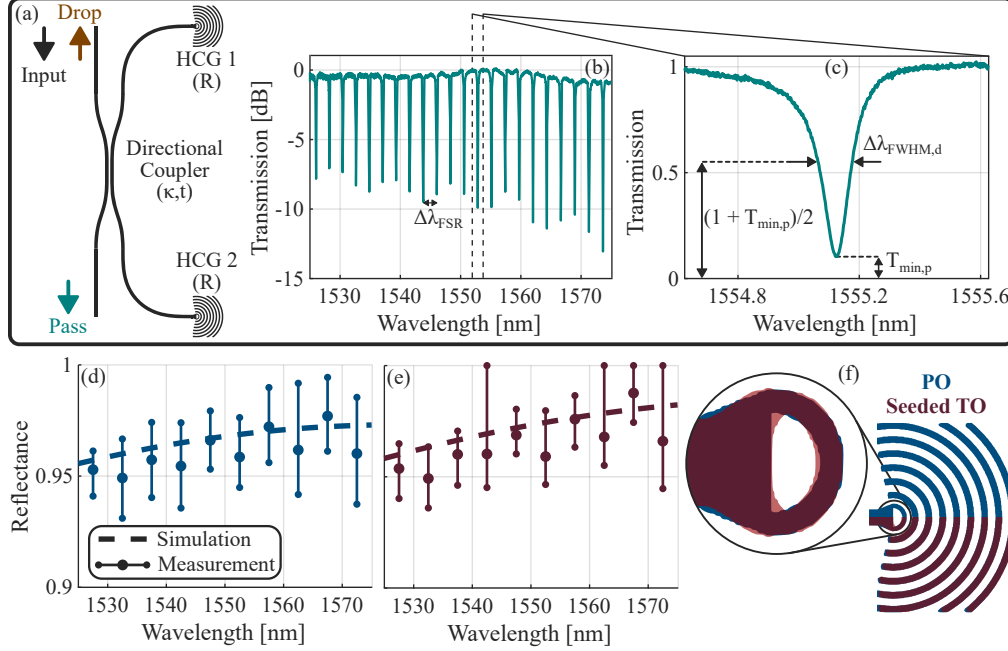


Fig. 7. (a) Resonator structure measured to determine the reflectance of the high contrast grating (HCG). (b,c) Measured pass-port transmission spectrum of the resonator with marked FSR ($\Delta\lambda_{FSR}$), drop-port FWHM ($\Delta\lambda_{FWHM,d}$), and pass-port minimum transmission ($T_{min,p}$). The simulated and measured reflectance spectra are plotted for the parameter optimized (PO) (d) and seeded TO (e) variants. The measured reflectances at each resonance peak are binned in 5 nm intervals; the mean, min, and max of each bin are shown. (f) Comparison of PO and seeded TO device geometries.

reflectance (R) is related to the drop port FWHM ($\Delta\lambda_{FWHM,d}$), the FSR ($\Delta\lambda_{FSR}$), and the directional coupler through-coupling coefficient (t) through the following equation [32, 41]:

$$\frac{\Delta\lambda_{FWHM,d}}{\Delta\lambda_{FSR}} = \frac{2}{\pi} \sin^{-1} \left(\frac{1 - Rt^2}{2\sqrt{R}t} \right) \quad (11)$$

The derivation for this can be found in the appendix A. Like the previous devices, the resonator pass-port test structure was implemented using the GF45CLO PDK grating couplers for I/O to be measured using a standard fiber array testing setup. The LUNA OVA 5100 was used for this measurement to ensure sufficient wavelength resolution (1.2 pm for the LUNA OVA compared to 10 pm for the tunable laser sweep). Resonant peaks in the transmission spectrum are identified using a peak-finding algorithm and used to calculate the FSR (Fig. 7b). Each peak is isolated and the FWHM is algorithmically calculated to determine the reflectance at each resonance peak (Fig. 7c). Test structures are measured of 5 separate chips from 2 wafer samples, the calculated reflectances are binned in 5 nm intervals, and the mean, min, and max of each bin are calculated and plotted along with the simulated reflectance (Fig. 7d,e).

Seeded TO had limited visible effect on the topology of the HCG, only modifying the hole at the waveguide-grating interface (Fig. 7f). This feature is critical to achieving maximum performance through shaping of the light entering the grating, but is limited by the minimum enclosed area constraint. The seeded TO modifications are demonstrated to improve performance in both simulation and measurement (Fig. 7d,e). This validates the effect that the minimal modifications made by seeded TO have on the performance of fabricated devices. The changes

made by seeded TO around the waveguide-grating interface are small enough that a designer may assume they will not be resolved in fabrication. However, the measured improvement of the fabricated device demonstrates small changes like this are critical to device performance.

5. Conclusion

We have demonstrated a seeded TO design methodology that allows for optimization of integrated photonic devices that yields improved performance over traditional TO. The seed is best chosen as a known functional device created via traditional TO, other optimization methods such as parameter or shape optimization, or from physics based models. Seeded TO relies on a blurring filter chosen to perturb the known structure seeking an optimized design. This new design methodology enables the creation of new, more robust algorithms to ensure the device meets DRC. We illustrated this optimization technique using four different test devices designed for a foundry process.

Seeded TO brings several important benefits to the integrated photonics inverse design community not seen in traditional topology optimization implementations. While traditional TO has the capability to discover non-intuitive device geometries, the optimal topology changes throughout the optimization as the design parameters binarize and DRC constraints are applied. This limits the ability of TO to find a strong optimal topology without careful hyperparameter tuning or a post-TO optimization scheme. Less hyperparameter tuning is required when using seeded TO resulting in fewer reloads throughout the optimization and a reduced total computational cost. This allows the designer to focus on the other aspects of the design process as hyperparameter tuning is often a tedious, time-consuming process. Seeded TO is compatible with any features implemented in TO including multi-layer and non-vertical sidewall optimization [20, 35]. A desirable consequence of seeded TO is the elimination of the periodic ripples that are commonly develop through traditional TO and have limited impact on device performance. This reduces the effect lithographic smoothing has on the device topology, resulting in greater alignment between measured and simulated performance.

There remain many opportunities for future work including exploring potential design techniques that can be used to create the seed (e.g. inverse design, shape optimization, physics-defined design, etc.). Designing a seed using using a physics-defined topology will allow for the optimization of large structures such as multimode interferometers, spot-size converters, and Bragg grating filters that have traditionally been difficult to inverse design due to simulation complexity. Additionally, there is scope to explore additional functionality in seeded TO such as creating algorithms that identify non-essential features of TO structures that can be removed to reduce device footprint. Intelligent implementation of non-gradient based design parameter modification has scope to significantly improve the performance of devices designed using TO.

Appendix A: High Contrast Grating Reflectance From Resonator Response

To measure the high contrast grating (HCG), a resonator was created with a directional coupler and 2 HCGs as mirrors (Fig. 8). This device acts as an add/drop ring resonator due to the counter-propagating light in the resonator. We derive the relation between the FWHM ($\Delta\lambda_{FWHM,d}$), FSR ($\Delta\lambda_{FSR}$), and directional coupler through-coupling coefficient (t) starting from the drop-port response:

$$\frac{E_{drop}}{E_{in}} = \frac{-\kappa^2 A^{\frac{1}{4}} e^{j\phi/2}}{1 - \sqrt{A} t^2 e^{j\phi}} \quad (12)$$

where $\kappa = \sqrt{1 - t^2}$ is the directional coupler cross-coupling coefficient, t is the directional coupler self-coupling coefficient (assumed real), A is the round-trip optical power attenuation, and ϕ is the round-trip optical phase [32]. The transmission to the drop port is:

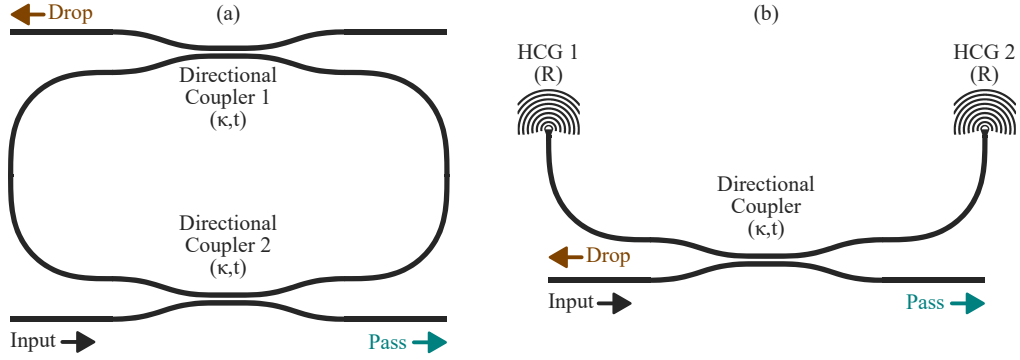


Fig. 8. (a) Add/drop ring resonator and (b) high contrast grating (HCG) resonator with input, through, and drop ports labeled.

$$T_d(\phi) = \frac{I_{drop}}{I_{in}} = \left| \frac{E_{drop}}{E_{in}} \right|^2 = \frac{\kappa^4 \sqrt{A}}{1 - t^2 \sqrt{A} (e^{j\phi} + e^{-j\phi}) + t^4 A} = \frac{\kappa^4 \sqrt{A}}{1 - 2t^2 \sqrt{A} \cos \phi + t^4 A} \quad (13)$$

The round-trip optical power loss is given by $A = R^2 e^{-\alpha L_{rt}}$ where R is the mirror reflectance and $e^{-\alpha L_{rt}}$ encapsulates the waveguide propagation loss. For this resonator, we assume the loss is all due to the mirror reflectance ($A = R^2$), the transmitted power becomes:

$$T_d(\phi) = \frac{R\kappa^4}{1 + R^2 t^4 - 2Rt^2 \cos \phi} \quad (14)$$

We can do the same calculation for the pass port, the transmission to the pass port is:

$$T_p(\phi) = \frac{t^2 + R^2 t^2 - 2Rt^2 \cos \phi}{1 + R^2 t^4 - 2Rt^2 \cos \phi} \quad (15)$$

The transmission to the pass and drop port are shown in Fig. 9. The maximum transmission at the drop port is:

$$T_{max,d} = \frac{R\kappa^4}{1 + R^2 t^4 - 2Rt^2} = \frac{R\kappa^4}{(1 - Rt^2)^2} \quad (16)$$

We can rewrite the drop port transmission as a function of the maximum transmission at the drop port:

$$T_d(\phi) = \frac{T_{d,max} (1 - Rt^2)^2}{1 + R^2 t^4 - 2Rt^2 (1 - 2 \sin^2(\phi/2))} = \frac{T_{d,max} (1 - Rt^2)^2}{(1 - Rt^2)^2 + 4Rt^2 \sin^2(\phi/2)} \quad (17)$$

We can define the contrast of the resonator F :

$$F = \frac{4Rt^2}{(1 - Rt^2)^2} \quad (18)$$

$$T_d(\phi) = \frac{T_{d,max}}{1 + F \sin^2(\phi/2)} \quad (19)$$

We can equate the drop port power to the maximum value to determine the phase bandwidth ($\Delta\phi_{FWHM,d}$):

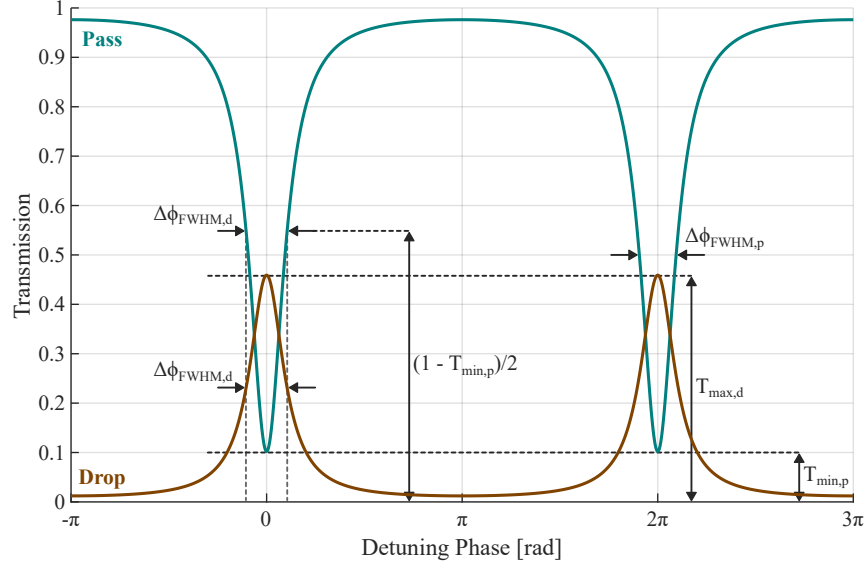


Fig. 9. Transmission spectrum of the add-drop ring resonator with labeled parameters.

$$T_d(\Delta\phi_{FWHM,d}/2) = \frac{T_{d,max}}{2} \rightarrow \frac{T_{d,max}}{1 + F \sin^2(\Delta\phi_{FWHM,d}/4)} = \frac{T_{d,max}}{2} \quad (20)$$

Simplifying:

$$\Delta\phi_{FWHM,d} = 4 \sin^{-1} \left(\frac{1}{\sqrt{F}} \right) = 4 \sin^{-1} \left(\frac{1 - Rt^2}{2\sqrt{Rt}} \right) \quad (21)$$

The phase bandwidth is related to the FWHM ($\Delta\lambda_{FWHM}$) and the FSR ($\Delta\lambda_{FSR}$) by [41]:

$$\frac{\Delta\lambda_{FWHM}}{\Delta\lambda_{FSR}} = \frac{\Delta\phi_{FWHM}}{2\pi} \quad (22)$$

This becomes:

$$\frac{\Delta\lambda_{FWHM,d}}{\Delta\lambda_{FSR}} = \frac{2}{\pi} \sin^{-1} \left(\frac{1 - Rt^2}{2\sqrt{Rt}} \right) \quad (23)$$

This equation relates the drop-port FWHM (measured at $T_p = (1 + T_{min,p})/2$ (see Fig. 9)), FSR, and directional coupler self-coupling coefficient to the mirror reflectance.

Funding. This material is based upon work supported in part by the National Science Foundation (NSF) Center “EPICA” under Grant No.1 2052808, <https://epica.research.gatech.edu/>. Any opinions, findings, and conclusions or recommendations expressed in this material are those of the author(s) and do not necessarily reflect the views of the NSF. JMH, CAK, JJW, PA, and SER were supported by the Georgia Electronic Design Center of the Georgia Institute of Technology.

Acknowledgments. This research was supported in part through research cyberinfrastructure resources and services provided by the Partnership for an Advanced Computing Environment (PACE) at the Georgia Institute of Technology, Atlanta, Georgia, USA [42]. The authors would like to thank GlobalFoundries for providing silicon fabrication through GF45CLO university program.

Disclosures. The authors declare no conflicts of interest.

Data availability. Data underlying the results presented in this paper are not publicly available at this time but may be obtained from the authors upon reasonable request.

References

1. A. M. Hammond, A. Oskooi, M. Chen, *et al.*, “High-performance hybrid time/frequency-domain topology optimization for large-scale photonics inverse design,” *Opt Express* **30**, 4467–4491 (2022).
2. S. Molesky, Z. Lin, A. Y. Piggott, *et al.*, “Inverse design in nanophotonics,” *Nat. Photonics* **12**, 659–670 (2018).
3. L. Su, R. Trivedi, N. V. Sapro, *et al.*, “Fully-automated optimization of grating couplers,” *Opt. express* **26**, 4023–4034 (2018).
4. R. E. Christiansen and O. Sigmund, “Inverse design in photonics by topology optimization: tutorial,” *JOSA B* **38**, 496–509 (2021).
5. G. Strang, *Computational science and engineering* (SIAM, 2007).
6. M. Liehr, M. Baier, G. Hoefler, *et al.*, *Foundry capabilities for photonic integrated circuits* (Elsevier, 2020), pp. 143–193.
7. A. M. Hammond, A. Oskooi, S. G. Johnson, and S. E. Ralph, “Photonic topology optimization with semiconductor-foundry design-rule constraints,” *Opt Express* **29**, 23916–23938 (2021).
8. R. P. Pesch, A. Khurana, J. B. Slaby, *et al.*, “Analysis of local optimization behavior: Toward a novel inverse design paradigm,” (2023).
9. J. M. Hiesener, J. B. Slaby, A. Khurana, *et al.*, “On intelligent inverse-design: Optimizing compact integrated photonic structures,” (2024).
10. J. M. Hiesener, R. P. Pesch, and S. E. Ralph, “On topology optimization strategies for ultra-compact high contrast grating design,” *IEEE Photonics Technol. Lett.* (2024).
11. J. J. Wong, J. M. Hiesener, A. Khurana, and S. E. Ralph, “Design techniques for ultra-compact low-loss multimode bends,” (2024).
12. A. Michaels, M. C. Wu, and E. Yablonovitch, “Hierarchical design and optimization of silicon photonics,” *IEEE J. Sel. Top. Quantum Electron.* **26**, 1–12 (2019).
13. C. M. Lalau-Keraly, S. Bhargava, O. D. Miller, and E. Yablonovitch, “Adjoint shape optimization applied to electromagnetic design,” *Opt. express* **21**, 21693–21701 (2013).
14. A. F. Oskooi, D. Roundy, M. Ibanescu, *et al.*, “Meep: A flexible free-software package for electromagnetic simulations by the fdtd method,” *Comput. Phys. Commun.* **181**, 687–702 (2010).
15. D. Vercruyse, N. V. Sapro, L. Su, *et al.*, “Analytical level set fabrication constraints for inverse design,” *Sci. reports* **9**, 8999 (2019).
16. M. Zhou, B. S. Lazarov, F. Wang, and O. Sigmund, “Minimum length scale in topology optimization by geometric constraints,” *Comput. Methods Appl. Mech. Eng.* **293**, 266–282 (2015).
17. A. Y. Piggott, E. Y. Ma, L. Su, *et al.*, “Inverse-designed photonics for semiconductor foundries,” *Acs Photonics* **7**, 569–575 (2020).
18. A. Y. Piggott, J. Petykiewicz, L. Su, and J. Vučković, “Fabrication-constrained nanophotonic inverse design,” *Sci. reports* **7**, 1786 (2017).
19. A. Messac, “Physical programming-effective optimization for computational design,” *AIAA journal* **34**, 149–158 (1996).
20. M. J. Probst, A. Khurana, J. B. Slaby, *et al.*, “Fabrication tolerant multi-layer integrated photonic topology optimization,” *Opt. Express* **32**, 31448–31462 (2024).
21. O. Sigmund and K. Maute, “Topology optimization approaches: A comparative review,” *Struct. multidisciplinary optimization* **48**, 1031–1055 (2013).
22. F. Wang, B. S. Lazarov, and O. Sigmund, “On projection methods, convergence and robust formulations in topology optimization,” *Struct. multidisciplinary optimization* **43**, 767–784 (2011).
23. R. E. Christiansen, J. Vester-Petersen, S. P. Madsen, and O. Sigmund, “A non-linear material interpolation for design of metallic nano-particles using topology optimization,” *Comput. Methods Appl. Mech. Eng.* **343**, 23–39 (2019).
24. M. Chen, R. E. Christiansen, J. A. Fan, *et al.*, “Validation and characterization of algorithms and software for photonics inverse design,” *J. Opt. Soc. Am. B* **41** (2024).
25. A. Oskooi, “Imageruler,” (2024).
26. J. B. Slaby, A. M. Hammond, and S. E. Ralph, “Low-loss high-density inverse-designed structures for high power signal routing on integrated silicon photonics foundry platforms,” (2023).
27. A. Khurana, J. B. Slaby, A. M. Hammond, and S. E. Ralph, “Inverse-designed photonic polarization control for high-density integration on foundry platforms,” in *2023 IEEE Silicon Photonics Conference (SiPhotonics)*, (2023), pp. 1–2.
28. K. R. Mojaver, S. M. R. Safaee, S. S. Morrison, and O. Liboiron-Ladouceur, “Recent advancements in mode division multiplexing for communication and computation in silicon photonics,” *J. Light. Technol.* (2024).
29. C. D. Truong, D. Nguyen Thi Hang, H. Chandralahim, and M. T. Trinh, “On-chip silicon photonic controllable 2×2 four-mode waveguide switch,” *Sci. Reports* **11**, 897 (2021).
30. K. Y. Yang, C. Shirpurkar, A. D. White, *et al.*, “Multi-dimensional data transmission using inverse-designed silicon photonics and microcombs,” *Nat. communications* **13**, 7862 (2022).
31. M. Eppenberger, A. Messner, P. Wintermeyer, *et al.*, “Labext - laboratory experiment tool,” (2021).

32. L. Chrostowski and M. Hochberg, *Silicon photonics design: from devices to systems* (Cambridge University Press, 2015).
33. X. Wang, W. Shi, M. Hochberg, *et al.*, "Lithography simulation for the fabrication of silicon photonic devices with deep-ultraviolet lithography," (2012).
34. Y. Xing, J. Dong, U. Khan, and W. Bogaerts, "Capturing the effects of spatial process variations in silicon photonic circuits," *ACS Photonics* **10**, 928–944 (2022).
35. A. M. Hammond, J. B. Slaby, M. J. Probst, and S. E. Ralph, "Multi-layer inverse design of vertical grating couplers for high-density, commercial foundry interconnects," *Opt Express* **30**, 31058–31072 (2022).
36. H. Zafar and M. F. Pereira, "Recent progress in light polarization control schemes for silicon integrated photonics," *Laser & Photonics Rev.* p. 2301025 (2024).
37. D. Dai, L. Liu, S. Gao, *et al.*, "Polarization management for silicon photonic integrated circuits," *Laser & Photonics Rev.* **7**, 303–328 (2013).
38. A. Kaushalram, J. M. Hiesener, C. A. Kaylor, and S. E. Ralph, "High dispersion in hybridized modes of silicon photonic devices compatible with a foundry platform," (2024).
39. J. Pita, F. Nabki, and M. Ménard, "Inverse-designed silicon nitride reflectors," *Opt. Lett.* **49**, 786–789 (2024).
40. S. Gao, Y. Wang, K. Wang, and E. Skafidas, "High contrast circular grating reflector on silicon-on-insulator platform," *Opt. Lett.* **41**, 520–523 (2016).
41. V. Van, *Optical microring resonators: theory, techniques, and applications* (CRC Press, 2016).
42. PACE, *Partnership for an Advanced Computing Environment (PACE)* (2017).